European Journal of
Mineralogy
Open Access

Equation of state and high-pressure
phase behaviour of SrCO₃

Nicole Biedermann[1,2], **Elena Bykova**[3], **Wolfgang Morgenroth**[2,4], **Ilias Efthimiopoulos**[5], **Jan Mueller**[5],
Georg Spiekermann[2,6], **Konstantin Glazyrin**[7], **Anna Pakhomova**[7], **Karen Appel**[1], and **Max Wilke**[2]

[1]European XFEL, Schenefeld, Germany
[2]Institute for Geosciences, University of Potsdam, Potsdam-Golm, Germany
[3]Geophysical Laboratory, Carnegie Institution of Washington, Washington, D.C., USA
[4]c/o European Synchrotron Radiation Facility ESRF, Grenoble, France
[5]GFZ German Research Center for Geosciences, Potsdam, Germany
[6]Institute of Geochemistry and Petrology, ETH Zürich, Zürich, Switzerland
[7]Deutsches Elektronen Synchroton DESY, Hamburg, Germany

Correspondence: Nicole Biedermann (nicole.biedermann@xfel.eu)

Abstract. The high-pressure phase transition of strontianite ($SrCO_3$) was investigated at ambient temperature by means of powder and single-crystal X-ray diffraction. The samples were compressed in a diamond anvil cell to a maximum pressure of 49 GPa. Structure refinements confirm the existence of $SrCO_3$ in the low pressure aragonite-type phase *Pmcn* (62) up to about 26 GPa. Above this pressure, $SrCO_3$ transforms into a high-pressure phase with post-aragonite crystal structure *Pmmn* (59). Fitting the volume extracted from the compression data to the third-order Birch–Murnaghan equation of state for the low-pressure phase of $SrCO_3$ yields $K_0 = 62.7(6)$ GPa and $K_0' = 3.2(1)$, and for the high-pressure phase this yields $K_0 = 103(10)$ GPa and $K_0' = 2.3(6)$. The unit cell parameters change non-uniformly, with the *c* axis being 4 times more compressible than the *a* and *b* axes. Our results unequivocally show the existence of a *Pmmn* structure in $SrCO_3$ above 26 GPa and provide important structural parameters for this phase.

1 Introduction

Carbonates play a key role in the chemistry and dynamics of our planet. They are directly connected to the CO_2 budget of our atmosphere and have a great impact on the deep carbon cycle (Li et al., 2019; McCammon et al., 2020). Moreover, it is believed that more than 90 % of the planet's carbon content is stored in the Earth's deep interior (Javoy, 1997; Dasgupta and Hirschmann, 2010; Kelemen and Manning, 2015). Indirect evidence for the presence of a deep carbon cycle is given by the existence of carbonatite melts causing metasomatism in the upper mantle (Litasov et al., 2013), by CO_2 in peridotitic and eclogitic systems with implications for deep melting of subducting slabs (Ghosh et al., 2009; Litasov, 2011; Thomson et al., 2016), by mantle minerals (e.g. clinopyroxene, olivine, garnet) hosting carbon-bearing inclusions (Korsakov and Hermann, 2006; Shcheka et al., 2006), and the

formation of diamonds. Several studies performed under the conditions of the Earth's mantle showed that carbon is incorporated in carbonates, which are stable phases at such conditions in equilibrium with other mineral phases (Isshiki et al., 2004; Merlini et al., 2012a,b; Boulard et al., 2015; Bayarjargal et al., 2018; Santos et al., 2019). Findings of carbonate inclusions in diamonds from the upper mantle and transition zone further substantiate the existence of carbonates in the deep Earth (Sobolev et al., 1998; Wirth et al., 2009; Brenker et al., 2007; Kaminsky et al., 2009).

The most abundant carbonates entering the subduction zone are Ca, Mg, and Fe carbonates. At the pressure–temperature (PT) conditions expected for subduction zones and the Earth's mantle, carbonates undergo pressure- and temperature-induced structural changes: $CaCO_3$, for instance, undergoes several phase transitions, some of them be-

coming more relevant to Earth's mantle conditions (Martinez et al., 1996; Santillán and Williams, 2004; Ono et al., 2005a; Oganov et al., 2006; Bayarjargal et al., 2018); other studies have shown the stability and phase transition of dolomite (Zucchini et al., 2017; Solomatova and Asimow, 2017; Efthimiopoulos et al., 2017), which is thought to be the main carbonate phase in subducting slabs. Regarding $CaCO_3$, numerous studies on the phase behaviour of aragonite-type $CaCO_3$ at high pressure reported a phase transition from orthorhombic aragonite (space group $Pmcn$) into monoclinic $CaCO_3$-VII at around 30 GPa and into post-aragonite structure $Pmmn$ at around 40 GPa (Gavryushkin et al., 2017; Bayarjargal et al., 2018).

Meanwhile, strontianite ($SrCO_3$-I), which is isostructural to aragonite at room pressure and room temperature conditions and very common in natural carbonates, is considered to have similar phase transitions but is at a lower pressure compared to aragonite due to the larger ionic radius of Sr^{2+} (1.31 Å) in comparison with Ca^{2+} (1.18 Å) (Shannon, 1976). Recent findings on mineral inclusions in transition zone diamonds showed significant amounts of strontium (Brenker et al., 2007; Kaminsky, 2012), which motivated our investigations of $SrCO_3$ as a possible stable phase in the deep Earth.

Whilst most of the physical properties of $SrCO_3$ are well known at ambient conditions (Villiers, 1971; Antao and Hassan, 2009; Nguyen-Thanh et al., 2016; Biedermann et al., 2017b), they have rarely been measured by powder X-ray diffraction at high pressure (Ono et al., 2005b; Wang et al., 2015), with some of them being based on density functional theory (DFT) calculations (Biedermann et al., 2017a; Efthimiopoulos et al., 2019). However, up to now, no single-crystal X-ray diffraction data were measured on $SrCO_3$, thus making it difficult to analyse structural changes at the conditions of the Earth's mantle. At ambient pressure, $SrCO_3$ has an aragonite-type crystal structure with space group $Pmcn$ (62). This crystal structure consists of planar trigonal $[CO_3]^{2-}$ oxyanions parallel to (001). The cations (e.g. Sr^{2+}) are surrounded by six CO_3^{2-} ions in a trigonal prismatic arrangement parallel to the c axis (see Fig. 8a), whereas the carbonate groups are octahedrally surrounded by six cations. The higher coordination number of the cation in the aragonite-group minerals correlates with a larger ionic radius (e.g. Sr^{2+}, Ba^{2+}, Pb^{2+}) compared to the calcite-group minerals, where the cation is only coordinated six-fold by the oxygen atoms.

A few studies on the pressure-induced phase transitions in $SrCO_3$ have been performed (Lin and Liu, 1997; Arapan and Ahuja, 2010; Wang et al., 2015; Biedermann et al., 2017a; Efthimiopoulos et al., 2019). They partially disagree regarding both the stability field and the structure of the high-pressure phases. Lin and Liu (1997) suggested a phase transition of $SrCO_3$ to post-aragonite between 32 and 35 GPa by Raman spectroscopy and proposed a space group setting of $P2_122$ for this phase. In comparison, Ono et al. (2005b) observed a post-aragonite phase by powder X-ray

diffraction of $SrCO_3$ already at 14.5 GPa and at 40 GPa for $CaCO_3$ (Ono et al., 2005a). In a later study, Ono (2007) could show that the post-aragonite modification in $BaCO_3$ has to be the same post-aragonite structure as $CaCO_3$ and $SrCO_3$ and had to be described in space group setting $Pmmn$. More recently, Wang et al. (2015) reported a possible high-pressure-induced transition at room temperature of $SrCO_3$ from $Pmcn$ to $P2_12_12$ between 22.2 and 26.9 GPa and of $BaCO_3$ from $Pmcn$ to $Pmmn$ between 9.8 and 11.2 GPa. A similar pressure range for a transition to the post-aragonite phase in $SrCO_3$ was proposed by Biedermann et al. (2017a) using experimental and computational Raman spectroscopy. Later on, the boundary of this phase transition was extended to high-temperature conditions using mid-infrared absorbance and Raman spectroscopy in combination with DFT-based calculations (Efthimiopoulos et al., 2019).

The variety of experimental conditions and techniques in the cited studies leads to results that are difficult to compare and sometimes even contradictory. To clarify these controversies we investigated the structure of pure $SrCO_3$ up to 49 GPa at ambient temperature by powder and single-crystal X-ray diffraction. This method allows us to precisely determine the crystal structure and to finally resolve the disagreement concerning the correct space group symmetry for the post-aragonite phase.

2 Methods

2.1 Synthesis of sample material

For powder X-ray diffraction experiments, we used commercial $SrCO_3$ powder from Sigma Aldrich Chemical Company (99.995 % purity). The single crystals of pure $SrCO_3$ strontianite were grown in a Walker-type multi-anvil apparatus at 4 GPa and 1273 K for 24 h using the same $SrCO_3$ powder as a starting material. The same synthesis has been used in previous studies (Biedermann et al., 2017a,b). The chemical composition of the synthesized sample was determined using a JEOL Hyperprobe JXA-8500F with a field emission cathode at the GFZ Potsdam. Analysis was conducted with an acceleration voltage of 15 kV, a 10 nA beam current, and a < 10 μm focused beam size. As reference-standard materials we used dolomite for CaO and strontianite for SrO. The chemical analysis indicated a concentration for Ca^{2+} below the detection limit of 130 ppm (see the Supplement for electron microprobe analysis). In addition, the morphology and chemical composition of the single crystals were studied with scanning electron microscopy. Most of the synthesized single crystals of $SrCO_3$ were twinned, which is very common for aragonite-type carbonates, as they exhibit pseudo-hexagonal morphologies with a mirror plane (110) as a twin plane (Bragg, 1924).

2.2 High-pressure X-ray diffraction experiments

2.2.1 Powder X-ray diffraction experiments

For high-pressure X-ray diffraction studies, $SrCO_3$ powder was pressurized to 49 GPa in a membrane-driven Mao–Bell-type diamond anvil cell (Mao and Hemley, 1997) equipped with 400 µm culets. Drilled pre-indented rhenium gaskets with a hole diameter of 200 µm served as sample chambers. The pressure-transmitting medium (PTM) neon and a ruby sphere were loaded in addition to the sample. The pressure in the cell was measured with an online HR-2000 spectrometer (Ocean Optics) using the R_1-line fluorescence band shift of ruby described by Mao et al. (1986) directly before and after each measurement, where the average is used as the experimental pressure. In addition, the equation of state of neon was used for additional pressure calibration (Hemley et al., 1989). The powder and single-crystal XRD experiments were carried out at beamline P02.2 at PETRA III, DESY (Hamburg) (Liermann et al., 2015). The X-ray wavelength was $\lambda = 0.2906$ Å, and the beam size was 2×2 µm² at full width at half maximum (FWHM). The calibration of the wavelength and the sample-to-detector distance was performed using standard CeO_2 powder. For data collection, we used a fast flat panel detector XRD1621 from Perkin Elmer (2048 pixels $\times$ 2048 pixels with 200×200 µm² pixel size). The two-dimensional X-ray images were integrated using the Fit2D programme (Hammersley, 2016). Refinements of the powder X-ray diffraction data were performed using the GSAS and EXPGUI software packages (Larson and Von Dreele, 2004).

2.2.2 Single-crystal X-ray diffraction experiments

In the case of high-pressure single crystal X-ray diffraction experiments, a small crystal of $SrCO_3$ (25–30 µm in diameter and 10 µm thickness), a piece of tungsten (~ 10 µm in diameter) and a ruby sphere (~ 10 µm in diameter) were placed into a 150 µm wide cylindrical chamber drilled in a pre-indented rhenium gasket. We used the same type of membrane-driven diamond anvil cells as in the case of powder samples but using diamonds with a smaller culet size of 300 µm. Again, neon was loaded into the cell as a pressure-transmitting medium. The single crystal was pressurized up to pressures of 26.3 GPa. A picture of the single crystal loaded into the cell and compressed to 25.9 GPa is shown in Fig. 1.

The intensities of the reflections for the $SrCO_3$ single crystal were integrated in steps of 0.5° over the entire opening angle of the cell of 54°. At each pressure point, additional X-ray diffraction wide images (from -27 to $+27$° in the rotation axis) were collected to confirm the data quality. The instrument model of the experimental geometry (sample-to-detector distance, the detector's origin, offsets of the goniometer angles, and rotation of the X-ray beam and the detector around the in-
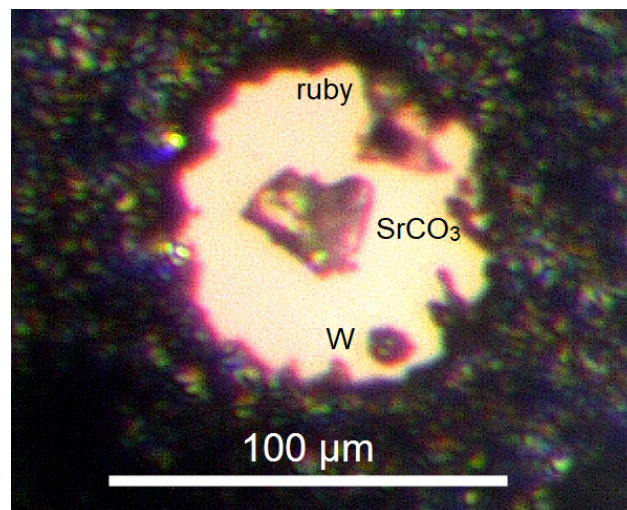

Figure 1. Diamond anvil cell at 25.9 GPa loaded with a single crystal of SrCO₃, with neon as a pressure-transmitting medium, a ruby sphere, and a piece of tungsten. The beam size was 2 µm × 2 µm FWHM.

Table 1. Observed d spacings of the post-aragonite phase SrCO₃-II at 26.3 GPa and room temperature in comparison with those from previous work (Ono et al., 2005b).

hkl	This study d_{obs} [Å] (26.3 GPa)	Ono et al. (2005b) d_{obs} [Å] (14.5 GPa)
001	4.2320	4.3106
110	3.3436	3.4197
011	3.2136	3.2750
101	3.0966	3.1644
111	2.6236	2.6803
020	2.4695	2.5210
200	2.2715	2.3260
021	2.1329	2.0477
121	1.9307	1.9720
102	1.9181	1.9545
211	1.5849	1.8964

strument axis) was calibrated against an orthoenstatite reference crystal: $(Mg_{1.93}Fe_{0.06})(Si_{1.93}Al_{0.06})O_6$, $Pbca$; $a = 18.2391(3)$ Å; $b = 8.8117(2)$ Å; $c = 5.18320(10)$ Å. The processing of XRD data (the unit cell determination and integration of the reflection intensities) was performed using CrysAlis PRO software (Rigaku Oxford Diffraction, 2019). Indexing of the unit cell was carried out on about 30 reflections manually selected in the reciprocal space viewer (Ewald explorer implemented in CrysAlis PRO software). The reflections were selected in order to determine a 3D lattice in the reciprocal space. The identified unit cell parameters were then refined on the whole set of reflections at the end of the integration.
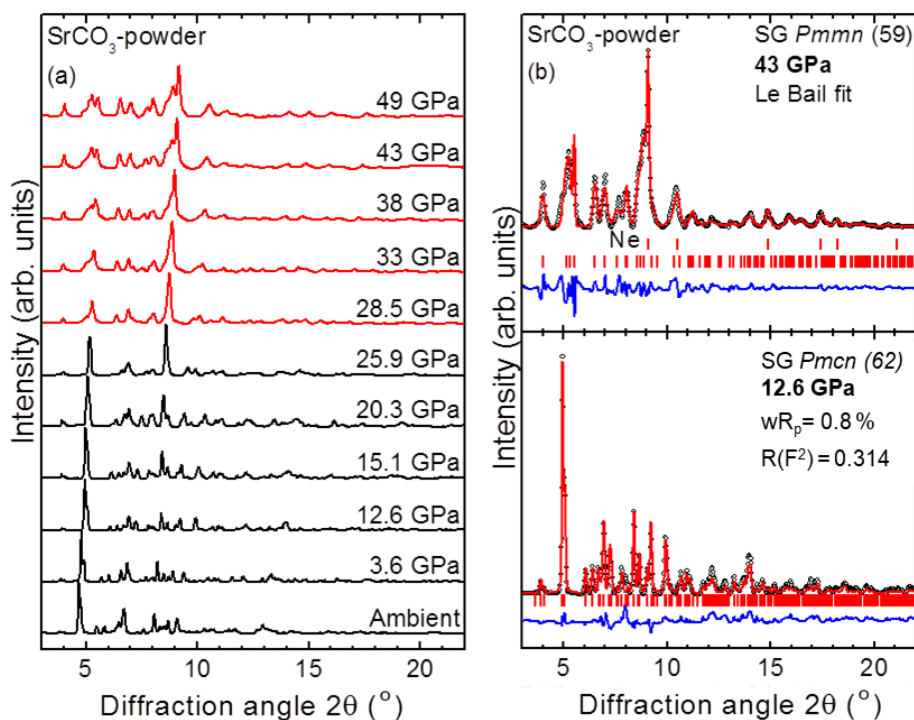
Figure 2. (a) Powder XRD patterns of SrCO₃ at various pressures ($T = 300$ K; $\lambda = 0.2906$ Å). The different phases are indicated by black (SrCO₃-I) and red (SrCO₃-II) colours. **(b)** Refined XRD patterns for the aragonite-type SrCO₃-I phase (12.6 GPa, Rietveld, bottom) and for SrCO₃-II (43 GPa, Le Bail, top). Dots correspond to the measured spectra and the solid red lines represent the best refinements. The difference curves between the measured and the refined patterns are depicted as well (blue curves). Vertical ticks mark the Bragg peak positions.

Table 2. Pressure dependence of lattice parameters of SrCO₃ at room temperature derived from powder X-ray diffraction.

P [GPa]	a [Å]	b [Å]	c [Å]	V [Å³]
SrCO₃-I in *Pmcn*				
0.0001	5.126(1)	8.472(2)	6.061(1)	263.21(15)
3.6(1)	5.057(1)	8.358(2)	5.840(1)	246.81(15)
12.6(2)	4.978(1)	8.182(2)	5.419(1)	220.73(15)
15.1(2)	4.957(1)	8.121(2)	5.337(1)	216.94(15)
20.3(2)	4.929(1)	8.017(2)	5.186(1)	209.85(15)
25.9(3)	4.892(1)	7.878(2)	5.037(1)	202.32(15)
SrCO₃-II in *Pmmn*				
28.5(3)	4.521(1)	4.918(1)	4.219(1)	93.79(8)
33(1)	4.459(1)	4.879(1)	4.194(1)	91.25(8)
38(1)	4.393(1)	4.845(1)	4.171(1)	88.79(8)
43(1.5)	4.325(1)	4.811(1)	4.151(1)	86.39(8)
49(2)	4.244(1)	4.782(1)	4.127(1)	83.75(8)

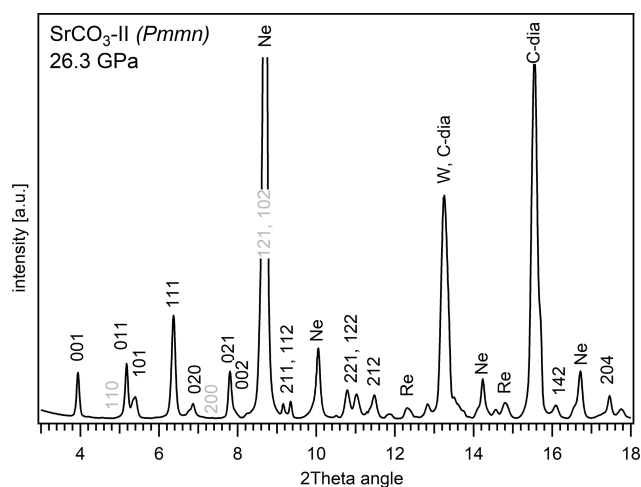Errors in parentheses are a single standard deviation.

Figure 3. A representative XRD pattern of post-aragonite SrCO₃-II obtained from single-crystal data at 26.3 GPa derived from continuous rotation around one axis from −27 to +27° (wide scan image). Reflections corresponding to SrCO₃-II that are absent, less intense, or overlaid are marked in grey.

The selected grain of SrCO$_3$ was a non-merohedral twin with following transformation:

$$\begin{pmatrix} -0.46 & -0.54 & 0 \\ 1.46 & -0.46 & 0 \\ 0 & 0 & 1 \end{pmatrix}. \tag{1}$$

The transformation corresponds to two oriented grains rotated by about 118° around the common c axis. Since the degree of overlap was small (less than 3 % of all reflections), no twin integration was applied for the SrCO$_3$-I phase data, and only the most intense grain (e.g. larger volume) was used for extraction of the reflection intensities. Overlapping 00l reflections were missing in the data set due to the orientation of the crystal in the diamond anvil cell (DAC) and its restricted opening angle. However, after the phase transition above 26 GPa we observed three twin domains related to a three-fold rotation along the a axis in SrCO$_3$-II. Due to a high degree of overlap between reflections (about 10 %), we applied simultaneous twin integration; however, further structure solution and refinement was performed using the data collected from the most intense twin component. Empirical absorption correction was applied using spherical harmonics, implemented in the SCALE3 ABSPACK scaling algorithm, which is included in the CrysAlis PRO software. The crystal structures of aragonite-type SrCO$_3$-I and post-aragonite SrCO$_3$-II were determined by the dual space method using SHELXT (Sheldrick, 2015) software. After the structure solution most of the atoms were found and the remaining were located from a series of difference Fourier maps. The crystal structures were refined against F^2 on all data by full-matrix least squares with the SHELXL (Sheldrick, 2015) software. The amount of the collected data allowed us to refine the structures in anisotropic approximation. Nevertheless, there is a pronounced elongation of anisotropic displacement parameters in SrCO$_3$-II along the [100] direction, due to three-fold twinning about the a axis. Details of crystal structure refinements of SrCO$_3$-I and SrCO$_3$-II are given in Table 3. The X-ray crystallographic coordinates have been deposited at the Inorganic Crystal Structure Database (ICSD) under deposition no. CSD1944794. This data can be obtained from CCDC's and FIZ Karlsruhe's free service for viewing and retrieving structures (http://www.ccdc.cam.ac.uk/structures/, last access: 28 October 2020).

3 Results and discussion

3.1 Phase transition of SrCO₃ during compression

Powder XRD patterns in the 2θ range 3–22° were collected upon compression up to 49(2) GPa and are presented in Fig. 2. No other peaks except those of the sample and the pressure transmitting medium neon (Ne) were observed. Peaks corresponding to the sample at ambient conditions were well indexed to the low-pressure aragonite

structure $Pmcn$ with the lattice parameters $a = 5.126(1)$ Å, $b = 8.472(2)$ Å, and $c = 6.061(1)$ Å and are in agreement with the literature (Wang et al., 2015; Villiers, 1971; Arapan and Ahuja, 2010; Antao and Hassan, 2009). As shown in Fig. 2, reflections of SrCO$_3$ shift to higher angles with increasing pressure and no structural transformation occurred until 25.9(3) GPa. A Rietveld refinement for the low-pressure aragonite-type SrCO$_3$-I phase up to a pressure of 15.1(2) GPa was used to calculate the lattice and structural parameters, including interatomic distances. Above 15 GPa, the broadening of the peaks does not allow reliable refinement of the structure; hence the method of Le Bail fitting was applied in order to derive lattice parameters from powder-XRD measurements between 15 and 49 GPa.

Some reflections of SrCO$_3$-I disappear, and new peaks appear at 28.5(3) GPa that could not be indexed using the metric of SrCO$_3$-I described in space group $Pmcn$. These new peaks increase in intensity at higher pressures and indicate that SrCO$_3$ has transformed into a post-aragonite phase. Our observations are in good agreement with powder X-ray diffraction studies from Wang et al. (2015) where a phase transition in SrCO$_3$ was observed between 22.2 and 26.9 GPa. In contrast, Ono et al. (2005b) proposed the presence of a post-aragonite phase in SrCO$_3$ already at 14.5 GPa and at high temperature, which was also indexed with the metric of SrCO$_3$-II described in space group $Pmmn$. For CaCO$_3$, a phase transformation into post-aragonite was observed at 40 GPa (Ono et al., 2005a) and for BaCO$_3$ at 10 GPa (Ono, 2007; Townsend et al., 2013). The pressure for a phase transition in SrCO$_3$ determined here lies in between these values and complies with the pressure–homologue rule according to which isostructural compounds often exhibit similar phase transitions but at lower pressures with increasing ionic radius (Ringwood, 1975).

Single-crystal X-ray diffraction experiments were performed from 0 to 26.3 GPa. In agreement with our results from powder X-ray diffraction, reflections of the single crystal can be unambiguously indexed with the same aragonite-type orthorhombic cell $Pmcn$ between 0 and about 21 GPa. Results taken at 26.3 GPa clearly indicate that SrCO$_3$ has fully transformed into post-aragonite phase with space group $Pmmn$, which is the stable phase of SrCO$_3$ at this higher pressure. The XRD pattern derived from a wide scan of the single crystal at this pressure is shown in Fig. 3. Additional peaks are indexed for rhenium, tungsten and the pressure transmitting medium neon. Fitted d spacings from this study at 26.3 GPa are given in Table 1 and are in good agreement with previous results from Ono et al. (2005b) at 14.5 GPa.

A comparison between the low-pressure phase and the post-aragonite phase is shown in Fig. 4. One can see that the a, b, and c axes in SrCO$_3$-I ($Pmcn$) correspond to the b, c, and a axes in SrCO$_3$-II ($Pmmn$). The phase transition from SrCO$_3$-I ($Pmcn$) to SrCO$_3$-II ($Pmmn$) is a first-order phase transition (Ono et al., 2005a) and is described by a shift of half of Sr^{2+} cations and CO$_3^{2-}$ anions along the [100] direc-

Table 3. Details of single-crystal structure refinements of SrCO$_3$-I and SrCO$_3$-II between 0.5 and 26.3 GPa.

P [GPa]	0.5(6)	5.2(4)	14.6(6)	20.6(4)	22.7(5)	25.9(4)	26.3(5)
Crystal data				SrCO$_3$-I			SrCO$_3$-II
Space group				*Pmcn* (no. 62)			*Pmmn* (no. 59)
a [Å]	5.1034(4)	5.0429(5)	4.9559(2)	4.9059(5)	4.8861(4)	4.8618(7)	4.543(2)
b [Å]	8.4056(8)	8.2858(9)	8.1986(5)	8.1932(8)	8.2025(8)	8.2078(12)	4.939(2)
c [Å]	6.0180(12)	5.7657(15)	5.3755(7)	5.1596(15)	5.0771(15)	4.985(2)	4.232(2)
V [Å^3]	258.15(6)	240.92(7)	218.41(3)	207.39(7)	203.48(7)	198.93(9)	94.97(8)
Z	4	4	4	4	4	4	2
$\langle$Sr1$\cdots$Sr1$\rangle$ [Å]	4.1326(4)	4.0077(6)	3.8399(4)	3.7761(7)	3.7626(6)	3.7432(10)	
$\langle$Sr1$\cdots$Sr1$\rangle$ in (001) [Å]	4.9174(4)	4.8507(5)	4.7908(4)	4.7752(6)	4.7739(5)	4.7699(8)	
Refinement							
θ range for data collection [°]	2.358 to 16.704	2.413 to 17.989	2.501 to 16.767	2.553 to 16.882	2.574 to 17.052	2.599 to 16.950	2.595 to 15.947
Completeness to $d =$ 0.8 Å	0.492	0.602	0.536	0.538	0.570	0.541	0.541
Index ranges	$-6 < h < 9$ $-10 < k < 15$ $-7 < l < 7$	$-9 < h < 9$ $-15 < k < 15$ $-7 < l < 7$	$-8 < h < 9$ $-15 < k < 12$ $-6 < l < 6$	$-9 < h < 7$ $-15 < k < 12$ $-5 < l < 5$	$-8 < h < 9$ $-15 < k < 14$ $-5 < l < 5$	$-5 < h < 5$ $-15 < k < 13$ $-5 < l < 5$	$-4 < h < 5$ $-7 < k < 8$ $-5 < l < 6$
Goodness of fit on F^2	1.064	1.015	0.943	0.989	1.037	1.033	1.369
Reflections collected	485	687	542	400	640	501	256
Independent reflections	355	421	325	289	319	299	142
No. of parameters	29	29	29	29	29	29	19
Final R indices [$I > 2\sigma(I)$], R_1/wR_2	0.0288/0.0696	0.0232/0.0611	0.0240/0.0629	0.0322/0.0951	0.0383/0.1050	0.0358/0.0944	0.0708/0.1922
R indices (all data) R_1/wR_2	0.0316/0.0739	0.0266/0.0654	0.0272/0.0677	0.0379/0.1020	0.0496/0.1087	0.0509/0.1112	0.0759/0.1955
R_{int}	0.013	0.016	0.020	0.017	0.047	0.022	0.014
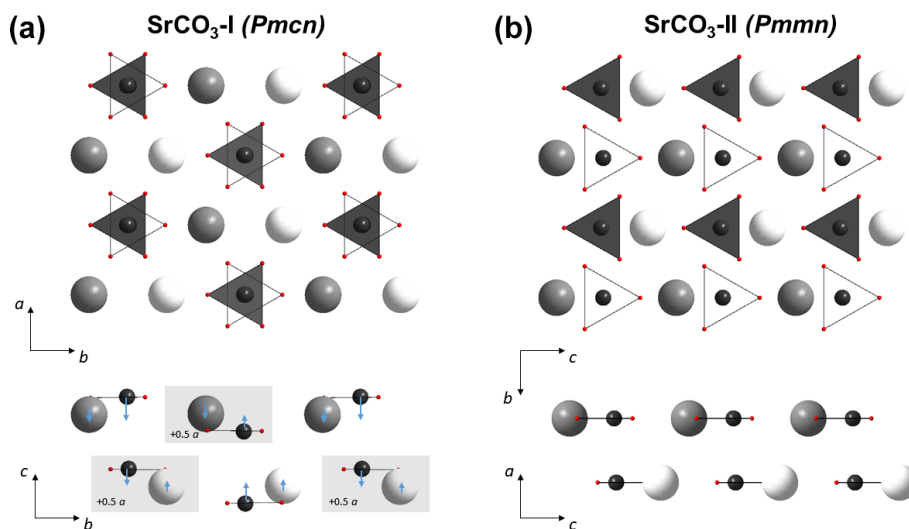
Figure 4. Crystal structures of SrCO$_3$-I **(a)** and SrCO$_3$-II **(b)**. Axis a, b, and c in SrCO$_3$-I (*Pmcn*) correspond to b, c and a axis in SrCO$_3$-II (*Pmmn*). Small-sized red spheres correspond to oxygen atoms, black spheres are carbon, CO$_3^{2-}$ are additionally highlighted as white and dark grey triangles, with different positions along the c axis in SrCO$_3$-I and along the a axis in SrCO$_3$-II. White and dark grey spheres are Sr^{2+}. During the phase transition from aragonite to post-aragonite half of Sr^{2+} and CO$_3^{2-}$ ions highlighted by grey rectangles shift by 0.5[100] and then the ions line up in the (001) plane (the directions of displacements are shown by small blue arrows).
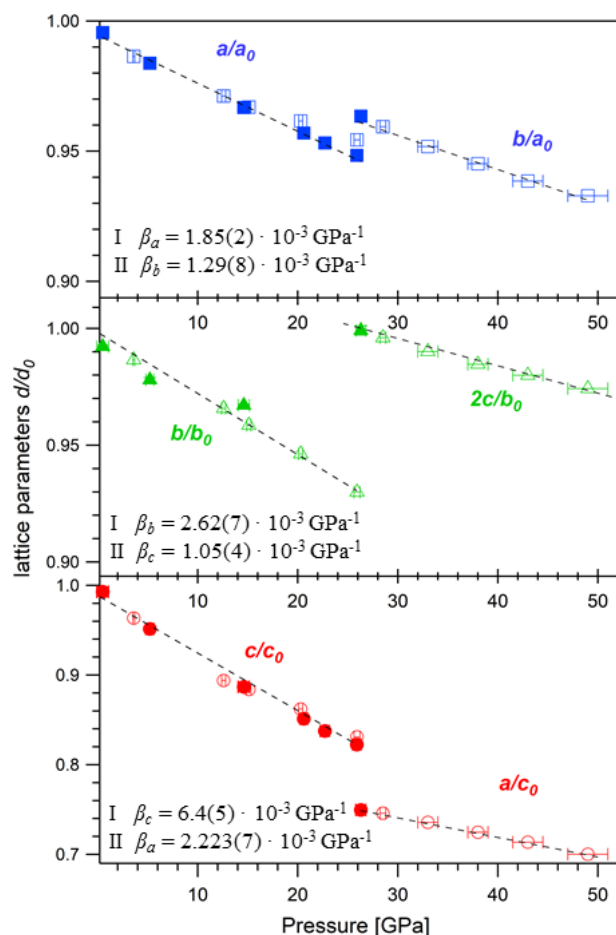
Figure 5. Compressibility of the unit cell parameters β_a, β_b, and β_c for SrCO₃-I and SrCO₃-II. Open symbols are data derived from powder samples, and solid symbols are from single-crystal X-ray diffraction. Note that the a, b, and c axes in SrCO₃-I (*Pmcn*) correspond to the b, c, and a axes in SrCO₃-II (*Pmmn*). The lattice parameters at ambient conditions are $a_0 = 5.126(1)$ Å, $b_0 = 8.472(2)$ Å, and $c_0 = 6.061(1)$ Å.

Figure 6. Evolution with pressure of the $\langle Sr \cdots Sr \rangle$ distances in the (001) plane (distance between two grey Sr spheres) and out of the (001) plane (distance between grey and white Sr spheres) in SrCO₃-I derived from single-crystal X-ray diffraction data. A schematic drawing of the crystal structure of SrCO₃-I in the (100) plane is given as an inset.

tion. At the same time, a shift by half of the translation of all Sr²⁺ cations and CO₃²⁻ anions accompanied with a small displacement along [001] occurs such that the cations and anions line up in one plane parallel to (001). These shifts result in more dense packing of cations and anions and in the increase of the Sr²⁺ coordination number from 9 to 12.

3.2 Compressibility of SrCO₃-I and SrCO₃-II

The refined unit cell parameters for the low-pressure phase strontianite (SrCO₃-I) and for the high-pressure phase SrCO₃-II obtained at different pressures are listed in Tables 2 and 3. The evolution of the lattice parameters with pressure is given in Fig. 5. Upon compression from 0.5 to 26 GPa, the axes of SrCO₃-I change anisotropically with the highest compressibility found in the direction of the c axis, which i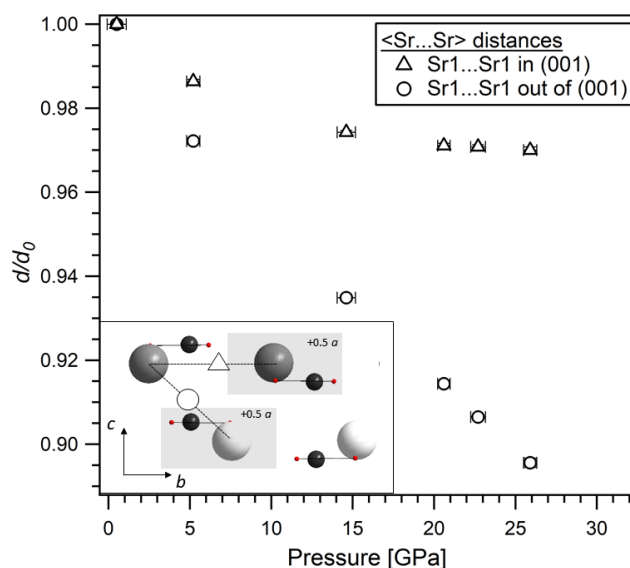s perpendicular to the carbonate groups. This anisotropic compression scheme is typical for aragonite-type carbonates (Townsend et al., 2013; Zhang et al., 2013) and reflects the incompressibility of the CO₃ groups in the (001) plane compared to the SrO₉ polyhedra. The determined lattice parameters for SrCO₃-I in this study exhibit quasi-linear pressure dependence with no obvious discontinuities. A linear fit of the given a/a_0, b/b_0, and c/c_0 values against pressure yields linear compressibilities of β_a, β_b, and β_c with $1.85(2) \times 10^{-3}$, $2.62(7) \times 10^{-3}$, and $6.4(5) \times 10^{-3}$ GPa⁻¹, respectively, and agrees well with data from Wang et al. (2015). Variations of the Sr⋯Sr distances in SrCO₃-I upon compression further substantiate an anisotropic compression behaviour, indicating anomalous contraction along the c axis (Fig. 6). Across phase transition at about 26 GPa, the length of the c axis ($\hat{=}a$ in SrCO₃-II) sharply decreases by $\sim 10\%$, whereas the b axis ($\hat{=}c$ in SrCO₃-II) increases. The lattice parameters of SrCO₃-II further decrease with pressure, albeit at lower rates, indicating that the structure of SrCO₃-II is less compressible than SrCO₃-I. The linear compressibilities of the high-pressure phase are found to be $2.223(7) \times 10^{-3}$ GPa⁻¹ for the a axis, $1.29(8) \times 10^{-3}$ GPa⁻¹ for the b axis, and $1.05(4) \times 10^{-3}$ GPa⁻¹ for the c axis.

The pressure dependence of the molar volume for SrCO₃-I and SrCO₃-II is shown in Fig. 7a. A plot of the Eulerian strain against the normalized pressure (f-F plot) (Fig. 7b) indicates that a third-order Birch–Murnaghan equation of state is necessary to fit the pressure–volume (P-V) data of SrCO₃, which
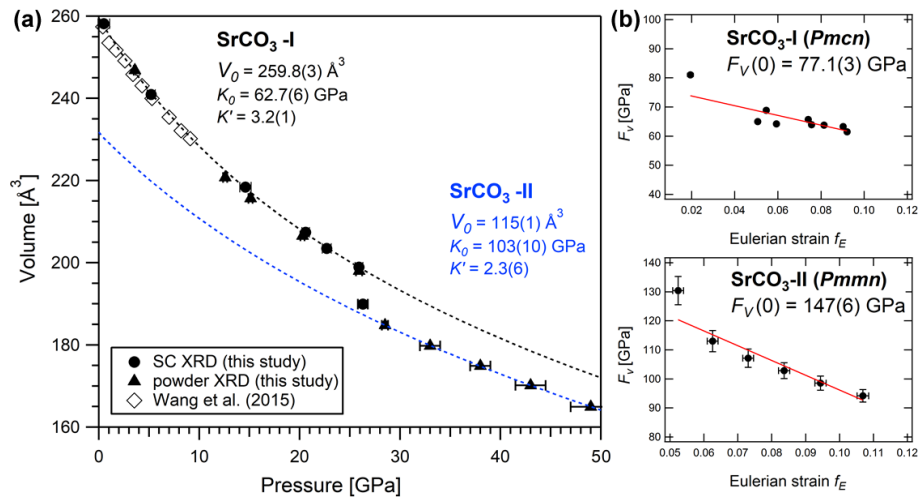
Figure 7. (a) Isothermal compression of the molar volume plotted together with the best fit following the Birch–Murnaghan equation of state for SrCO₃-I (dashed black line) and SrCO₃-II (dashed blue line). Open symbols are data from Wang et al. (2015) (with methanol and ethanol as PTM), and solid symbols are from this study. Note that for SrCO₃-II the depicted data points show the doubled values of the unit cell volume. **(b)** Normalized pressure (F_V) as a function of the Eulerian strain (f) for SrCO₃-I and SrCO₃-II, respectively. The solid red lines are the weighted linear fits to the data at $P > 3.6$ GPa.
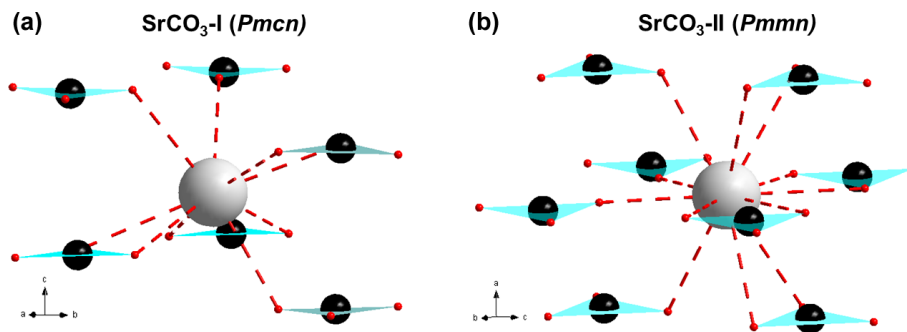
Figure 8. A fragment of SrCO₃-I **(a)** and SrCO₃-II **(b)** crystal structure at ambient pressure and at 26.3 GPa, respectively, showing Sr^{2+} ions (light grey sphere) surrounded by six CO_3^{2-} anions in the aragonite structure, whereas Sr^{2+} ions in the post-aragonite structure are surrounded by eight triangular CO_3^{2-} anions (C: dark grey spheres; O: red spheres).

is expressed as follows (Birch, 1947; Angel et al., 2014):

$$P(\text{GPa}) = 3K_0 f_E \left[(1 + 2f_E)^{\frac{5}{2}} \left(1 + \frac{3}{2}(K' - 4) f_E \right) \right], \quad (2)$$

with f_E as the Eulerian strain given by

$$f_E = \frac{1}{2} \left[(V_0/V)^{\frac{2}{3}} - 1 \right], \quad (3)$$

and where V_0, K_0, and K' are the (molar) volume, the isothermal bulk modulus, and its pressure derivative at room pressure, respectively. The programme EosFit7c (Angel et al., 2014) was used to fit the data. For the low-pressure phase strontianite (SrCO₃-I), the following EoS parameters were calculated: $V_0 = 259.8(3)$ Å³, $K_0 = 62.7(6)$ GPa, and $K_0' = 3.2(1)$. Values for K_0 are in good agreement with previous studies on strontianite (Wang et al., 2015; Biedermann et al., 2017b). The fit result for the high-pressure

phase SrCO₃-II yields $V_0 = 115(1)$ Å³, $K_0 = 103(10)$ GPa and $K_0' = 2.3(6)$, respectively. As indicated in Table 4, these values are between the values for BaCO₃-II, with $K_0 = 84(4)$ GPa (Ono, 2007), and for post-aragonite CaCO₃, with 127(14) GPa (Ono et al., 2005a), thus confirming a dependency on the cation radius.

3.3 Crystal structure of post-aragonite SrCO₃-II

A detailed refinement of the high-pressure phase was carried out on single crystal X-ray diffraction data at 26.3 GPa. We were able to refine the structure in the anisotropic approximation. Fractional atomic coordinates and anisotropic displacement parameters are shown in Table 5. At this pressure, the post-aragonite phase of SrCO₃ crystallizes in an orthorhombic unit cell with space group *Pmmn* (no. 59, origin choice 2) and with the following unit cell parameters: $a = 4.543(2)$ Å,

Table 4. Comparison of the literature data for aragonite-type (*Pmcn*) and post-aragonite (*Pmmn* or $P2_12_12$) carbonates at ambient conditions.

	V_0 [Å³]	K_0 [GPa]	K'_{T0}	References
Aragonite-type carbonates				
CaCO₃	227.5(8)	65(4)	4 (fixed)	Martinez et al. (1996)
	227.2(10)	67.1(63)	4.7(8)	Ono et al. (2005a)
	227.2(10)	73.1(22)	4 (fixed)	Ono et al. (2005a)
SrCO₃-I	258.4(3)	62(1)	4 (fixed)	Wang et al. (2015)
	258.4(1)	64(4)		Biedermann et al. (2017b)
	259.8(3)	62.7(6)	3.2(1)	This work
BaCO₃	303.8(1)	50.4(9)	1.9(4)	Holl et al. (2000)
	304.1(3)	44.3(8)	4 (fixed)	Holl et al. (2000)
	319.3	47.2	2.4	Ono et al. (2008)
	304.8(3)	48(1)	4 (fixed)	Wang et al. (2015)
post-aragonite carbonates				
CaCO₃ Post-aragonite	98(2)	127(14)	4 (fixed)	Ono et al. (2005a)
	102(3)	90(13)	4.94	Oganov et al. (2006)
	109.74	42(7)	7(1)	Oganov et al. (2006)
SrCO₃-II	115(1)	103(10)	2.3(6)	This work
	111(2)	101(16)	4 (fixed)	Ono et al. (2005b)
BaCO₃ post-aragonite	129.0(7)	84(4)	4 (fixed)	Ono (2007)
	128.1(5)	88(2)	4.8(3)	Townsend et al. (2013)

Table 5. Atomic coordinates and anisotropic displacement parameters U_{ij} [Å²] for post-aragonite SrCO₃-II at 26.3 GPa (space group *Pmmn*).

Site	Wyckoff position	x	y	z	U_{11}	U_{22}	U_{33}	U_{23}	U_{13}	U_{12}
Sr	*2b*	0.25	−0.25	0.6186(4)	0.036(2)	0.0096(8)	0.0152(10)	0	0	0
C	*2a*	0.25	0.25	0.991(4)	0.04(2)	0.010(5)	0.007(8)	0	0	0
O1	*2a*	0.25	0.25	0.682(3)	0.029(12)	0.005(4)	0.011(6)	0	0	0
O2	*4e*	0.25	0.025(2)	0.146(2)	0.026(11)	0.012(3)	0.009(4)	0.000(2)	0	0

$b = 4.939(2)$ Å, $c = 4.232(2)$ Å, and $V = 94.97(8)$ Å³. The atomic arrangement in post-aragonite SrCO₃-II adopts the structure type of the orthorhombic high-pressure form of RbNO₃-V (Kalliomäki and Meisalo, 1979). The Sr ion is located on a Wyckoff position *2b*, C is on a *2a* position, and O1 and O2 atoms occupy *2a* and *4e* positions, respectively (Table 5). The same crystal structure was already proposed for high-pressure modifications of CaCO₃ (Ono et al., 2005a) and for BaCO₃ (Ono, 2007; Townsend et al., 2013). However, there are also XRD data suggesting a trigonal symmetry for the post-aragonite phase in CaCO₃ (Santillán and Williams, 2004) and in BaCO₃ (Holl et al., 2000). When adapting the trigonal symmetry reported by Holl et al. (2000) some diffraction peaks of the high-pressure phase of SrCO₃ could not be indexed. We conclude that for SrCO₃ only an orthorhombic description of the crystal structure for the post-aragonite phase is possible.

The *Pmcn* to *Pmmn* transition of SrCO₃ is characterized by an increase of the coordination of Sr^{2+} from 9 to 12. The relative change in density across this transition is about 5 %. In the post-aragonite phase the Sr to O interatomic distances vary from 2.418(10) to 2.718(6) Å. Six oxygen atoms with shorter distances (2.418(10), 2.4842(19), and 2.613(10) Å) are located on a plane intersecting Sr, parallel to the *bc* plane. Three oxygen atoms are located below the plane, and three atoms are located above it. C to O distances in the high-pressure phase of SrCO₃ are 1.291(13) and 1.31(2) Å and identical within errors with data from Ono et al. (2005a) for CaCO₃.

4 Conclusions

Powder X-ray diffraction in combination with single-crystal X-ray diffraction was used for the first time to determine

the high-pressure phase behaviour of SrCO$_3$ up to 49 GPa at ambient temperature. We observed a transformation from strontianite (*Pmcn*) to post-aragonite SrCO$_3$-II (*Pmmn*) at around 26 GPa, which is in agreement with previous studies that used other techniques, e.g. Raman spectroscopy, to detect a phase transition in SrCO$_3$ (Biedermann et al., 2017a). We present reliable structural information for post-aragonite SrCO$_3$-II, including interatomic distances and anisotropic displacement parameters, and finally resolve the discussion about the correct space group setting of the post-aragonite phase in SrCO$_3$. Our results further confirm a bulk modulus of 62.7(6) GPa for strontianite (SrCO$_3$-I) and provide the first experimental data for the equation of state for the high-pressure phase SrCO$_3$-II with $V_0 = 115(1)$ Å^3, $K_0 = 103(10)$ GPa and $K_0' = 2.3(6)$.

References

Angel, R. J., Alvaro, M., and Gonzalez-Platas, J.: EosFit7c and a Fortran module (library) for equation of state calculations, Z. Kristallogr., 229, 405–419, https://doi.org/10.1515/zkri-2013-1711, 2014.

Antao, S. M. and Hassan, I.: The orthorhombic structure of CaCO$_3$, SrCO$_3$, PbCO$_3$ and BaCO$_3$: Linear structural trends, The Canadian Mineralogist, 47, 1245–1255, https://doi.org/10.3749/canmin.47.5.1245, 2009.

Arapan, S. and Ahuja, R.: High-pressure phase transformations in carbonates, Phys. Rev. B, 82, 184115, https://doi.org/10.1103/physrevb.82.184115, 2010.

Bayarjargal, L., Fruhner, C.-J., Schrodt, N., and Winkler, B.: CaCO$_3$ phase diagram studied with Raman spectroscopy at pressures up to 50 GPa and high temperatures and DFT modeling, Phys. Earth Planet. In., 281, 31–45, https://doi.org/10.1016/j.pepi.2018.05.002, 2018.

Biedermann, N., Speziale, S., Winkler, B., Reichmann, H. J., Koch-Müller, M., and Heide, G.: High-pressure phase behavior of SrCO$_3$: an experimental and computational Raman scattering study, Phys. Chem. Miner., 44, 335–343, https://doi.org/10.1007/s00269-016-0861-2, 2017a.

Biedermann, N., Winkler, B., Speziale, S., Reichmann, H. J., and Koch-Müller, M.: Single-crystal elasticity of SrCO$_3$ by Brillouin spectroscopy, High Pressure Res., 37, 181–192, https://doi.org/10.1080/08957959.2017.1289193, 2017b.

Birch, F.: Finite Elastic Strain of Cubic Crystals, Phys. Rev., 71, 809–824, https://doi.org/10.1103/physrev.71.809, 1947.

Boulard, E., Goncharov, A. F., Blanchard, M., and Mao, W. L.: Pressure-induced phase transition in MnCO$_3$ and its implications on the deep carbon cycle, J. Geophys. Res.-Sol. Ea., 120, 4069–4079, https://doi.org/10.1002/2015jb011901, 2015.

Bragg, W. L.: The structure of aragonite, Proceedings of the Royal Society of London. Series A, Containing Papers of a Mathematical and Physical Character, 105, 16–39, https://doi.org/10.1098/rspa.1924.0002, 1924.

Brenker, F. E., Vollmer, C., Vincze, L., Vekemans, B., Szymanski, A., Janssens, K., Szaloki, I., Nasdala, L., Joswig, W., and Kaminsky, F.: Carbonates from the lower part of transition zone or even the lower mantle, Earth Planet. Sci. Lett., 260, 1–9, https://doi.org/10.1016/j.epsl.2007.02.038, 2007.

Dasgupta, R. and Hirschmann, M. M.: The deep carbon cycle and melting in Earth's interior, Earth Planet. Sc. Let., 298, 1–13, https://doi.org/10.1016/j.epsl.2010.06.039, 2010.

Efthimiopoulos, I., Jahn, S., Kuras, A., Schade, U., and Koch-Müller, M.: Combined high-pressure and high-temperature vibrational studies of dolomite: phase diagram and evidence of a new distorted modification, Phys. Chem. Miner., 44, 465–476, https://doi.org/10.1007/s00269-017-0874-5, 2017.

Efthimiopoulos, I., Müller, J., Winkler, B., Otzen, C., Harms, M., Schade, U., and Koch-Müller, M.: Vibrational response of strontianite at high pressures and high temperatures and construction of P–T phase diagram, Phys. Chem. Miner., 46, 27–35, https://doi.org/10.1007/s00269-018-0984-8, 2019.

Gavryushkin, P. N., Martirosyan, N. S., Inerbaev, T. M., Popov, Z. I., Rashchenko, S. V., Likhacheva, A. Y., Lobanov, S. S., Goncharov, A. F., Prakapenka, V. B., and Litasov, K. D.: Aragonite-II and CaCO₃-VII: New High-Pressure, High-Temperature Polymorphs of CaCO₃, Cryst. Growth Des., 17, 6291–6296, https://doi.org/10.1021/acs.cgd.7b00977, 2017.

Ghosh, S., Ohtani, E., Litasov, K. D., and Terasaki, H.: Solidus of carbonated peridotite from 10 to 20 GPa and origin of magnesio-carbonatite melt in the Earth's deep mantle, Chem. Geol., 262, 17–28, https://doi.org/10.1016/j.chemgeo.2008.12.030, 2009.

Hammersley, A. P.: FIT2D: a multi-purpose data reduction, analysis and visualization program, J. Appl. Crystallogr., 49, 646–652, https://doi.org/10.1107/s1600576716000455, 2016.

Hemley, R. J., Zha, C. S., Jephcoat, A. P., Mao, H. K., Finger, L. W., and Cox, D. E.: X-ray diffraction and equation of state of solid neon to 110 GPa, Phys. Rev. B, 39, 11820–11827, https://doi.org/10.1103/physrevb.39.11820, 1989.

Holl, C. M., Smyth, J. R., Laustsen, H. M. S., Jacobsen, S. D., and Downs, R. T.: Compression of witherite to 8 GPa and the crystal structure of BaCO₃ II, Phys. Chem. Miner., 27, 467–473, https://doi.org/10.1007/s002690000087, 2000.

Isshiki, M., Irifune, T., Hirose, K., Ono, S., Ohishi, Y., Watanuki, T., Nishibori, E., Takata, M., and Sakata, M.: Stability of magnesite and its high-pressure form in the lowermost mantle, Nature, 427, 60–63, https://doi.org/10.1038/nature02181, 2004.

Javoy, M.: The major volatile elements of the Earth: Their origin, behavior, and fate, Geophys. Res. Lett., 24, 177–180, https://doi.org/10.1029/96gl03931, 1997.

Kalliomäki, M. S. and Meisalo, V. P. J.: Structure determination of the high-pressure phases RbNO₃-V, CsNO₃-III, and CsNO₃-IV, Acta Crystall. B-Stru., 35, 2829–2835, https://doi.org/10.1107/s0567740879010773, 1979.

Kaminsky, F.: Mineralogy of the lower mantle: A review of 'super-deep' mineral inclusions in diamond, Earth-Sci. Rev., 110, 127–147, https://doi.org/10.1016/j.earscirev.2011.10.005, 2012.

Kaminsky, F., Wirth, R., Matsyuk, S., Schreiber, A., and Thomas, R.: Nyerereite and nahcolite inclusions in diamond: evidence for lower-mantle carbonatitic magmas, Mineral. Mag., 73, 797–816, https://doi.org/10.1180/minmag.2009.073.5.797, 2009.

Kelemen, P. B. and Manning, C. E.: Reevaluating carbon fluxes in subduction zones, what goes down, mostly comes up, P. Natl. Acad. Sci. USA, 112, E3997–E4006, https://doi.org/10.1073/pnas.1507889112, 2015.

Korsakov, A. V. and Hermann, J.: Silicate and carbonate melt inclusions associated with diamonds in deeply subducted carbonate rocks, Earth Planet. Sc. Lett., 241, 104–118, https://doi.org/10.1016/j.epsl.2005.10.037, 2006.

Larson, A. C. and Von Dreele, R. B.: General structure analysis system (GSAS) (Report LAUR 86-748), Los Alamos National Laboratory, Los Alamos, New Mexico, 2004.

Li, J., Redfern, S. A., and Giovannelli, D.: Introduction: Deep carbon cycle through five reactions, Am. Mineral., 104, 465–467, https://doi.org/10.2138/am-2019-6833, 2019.

Liermann, H.-P., Konôpková, Z., Morgenroth, W., Glazyrin, K., Bednarčik, J., McBride, E. E., Petitgirard, S., Delitz, J. T., Wendt, M., Bican, Y., Ehnes, A., Schwark, I., Rothkirch, A., Tischer, M., Heuer, J., Schulte-Schrepping, H., Kracht, T., and Franz, H.: The Extreme Conditions Beamline P02.2 and the Extreme Conditions Science Infrastructure at PETRA III, J. Synchrotron Radiat., 22, 908–924, https://doi.org/10.1107/s1600577515005937, 2015.

Lin, C.-C. and Liu, L.-G.: Post-aragonite phase transitions in strontianite and cerussite: A high-pressure Raman spectroscopic study, J. Phys. Chem. Solids, 58, 977–987, https://doi.org/10.1016/s0022-3697(96)00201-6, 1997.

Litasov, K.: Physicochemical conditions for melting in the Earth's mantle containing a C–O–H fluid (from experimental data), Russ. Geol. Geophys., 52, 475–492, https://doi.org/10.1016/j.rgg.2011.04.001, 2011.

Litasov, K. D., Shatskiy, A., Ohtani, E., and Yaxley, G. M.: Solidus of alkaline carbonatite in the deep mantle, Geology, 41, 79–82, https://doi.org/10.1130/g33488.1, 2013.

Mao, H. K. and Hemley, R. J. M. A. L.: Diamond-cell research with synchrotron radiation, Advances in High Pressure Research, 29, 12–20, 1997.

Mao, H. K., Xu, J., and Bell, P. M.: Calibration of the ruby pressure gauge to 800 kbar under quasi-hydrostatic conditions, J. Geophys. Res., 91, 4673, https://doi.org/10.1029/jb091ib05p04673, 1986.

Martinez, I., Zhang, J., and Reeder, R. J.: In situ X-ray diffraction of aragonite and dolomite at high pressure and high temperature; evidence for dolomite breakdown to aragonite and magnesite, Am. Mineral., 81, 611–624, https://doi.org/10.2138/am-1996-5-608, 1996.

McCammon, C., Bureau, H., Cleaves, J. H., Cottrell, E., Dorfman, S. M., Kellogg, L. H., Li, J., Mikhail, S., Moussallam, Y., Sanloup, C., Thomson, A. R., and Brovarone, A. V.: Deep Earth carbon reactions through time and space, Am. Mineral., 105, 22–27, https://doi.org/10.2138/am-2020-6888ccby, 2020.

Merlini, M., Crichton, W. A., Hanfland, M., Gemmi, M., Muller, H., Kupenko, I., and Dubrovinsky, L.: Structures of dolomite at ultrahigh pressure and their influence on the deep carbon cycle, P. Natl. Acad. Sci. USA, 109, 13509–13514, https://doi.org/10.1073/pnas.1201336109, 2012a.

Merlini, M., Hanfland, M., and Crichton, W.: CaCO₃-III and CaCO₃-VI, high-pressure polymorphs of calcite: Possible host structures for carbon in the Earth's mantle, Earth Planet. Sc. Lett., 333-334, 265–271, https://doi.org/10.1016/j.epsl.2012.04.036, 2012b.

Nguyen-Thanh, T., Bosak, A., Bauer, J. D., Luchitskaia, R., Refson, K., Milman, V., and Winkler, B.: Lattice dynamics and elasticity of SrCO₃, J. Appl. Crystallogr., 49, 1982–1990, https://doi.org/10.1107/s1600576716014205, 2016.

Oganov, A. R., Glass, C. W., and Ono, S.: High-pressure phases of CaCO₃: Crystal structure prediction and experiment, Earth Planet. Sc. Lett., 241, 95–103, https://doi.org/10.1016/j.epsl.2005.10.014, 2006.

Ono, S.: New high-pressure phases in BaCO₃, Phys. Chem. Miner., 34, 215–221, https://doi.org/10.1007/s00269-006-0140-8, 2007.

Ono, S., Kikegawa, T., Oshishi, Y., and Tsuchiya, J.: Post-aragonite phase transformation in CaCO₃ at 40 GPa, Am. Mineral., 90, 667–671, https://doi.org/10.2138/am.2005.1610, 2005a.

Ono, S., Shirasaka, M., Kikegawa, T., and Ohishi, Y.: A new high-pressure phase of strontium carbonate, Phys. Chem. Miner., 32, 8–12, https://doi.org/10.1007/s00269-004-0428-5, 2005b.

Ono, S., Brodholt, J. P., and Price, G. D.: Phase transitions of BaCO₃ at high pressures, Mineral. Mag., 72, 659–665, https://doi.org/10.1180/minmag.2008.072.2.659, 2008.

Rigaku Oxford Diffraction: CrysAlis PRO software system, Version 1.171.40.57a, Rigaku Oxford Diffraction, Oxford, UK, 2019.

Ringwood, A.: Composition and petrology of the Earth's mantle, McGraw-Hill, New York, 618, 1975.

Santillán, J. and Williams, Q.: A high pressure X-ray diffraction study of aragonite and the post-aragonite phase transition in CaCO$_3$, Am. Mineral., 89, 1348–1352, https://doi.org/10.2138/am-2004-8-925, 2004.

Santos, S. S., Marcondes, M. L., Justo, J. F., and Assali, L. V.: Stability of calcium and magnesium carbonates at Earth's lower mantle thermodynamic conditions, Earth Planet. Sc. Lett., 506, 1–7, https://doi.org/10.1016/j.epsl.2018.10.030, 2019.

Shannon, R.: Revised Effective Ionic Radii and Systematic Studies of Interatomic Distances in Halides and Chalcogenides, Acta Crystall. A-Crys., 32, 751–767, https://doi.org/10.1107/S0567739476001551, 1976.

Shcheka, S. S., Wiedenbeck, M., Frost, D. J., and Keppler, H.: Carbon solubility in mantle minerals, Earth Planet. Sc. Lett., 245, 730–742, https://doi.org/10.1016/j.epsl.2006.03.036, 2006.

Sheldrick, G. M.: SHELXT – Integrated space-group and crystal-structure determination, Acta Crystallogr. A, 71, 3–8, https://doi.org/10.1107/s2053273314026370, 2015.

Sobolev, N. V., Yefimova, E. S., Channer, D. M. D., Anderson, P. F. N., and Barron, K. M.: Unusual upper mantle beneath Guaniamo, Guyana shield, Venezuela: Evidence from diamond inclusions, Geology, 26, 971–974, 1998.

Solomatova, N. V. and Asimow, P. D.: Ab initio study of the structure and stability of CaMg(CO$_3$)$_2$ at high pressure, Am. Mineral., 102, 210–215, https://doi.org/10.2138/am-2017-5830, 2017.

Thomson, A., Kohn, S., Bulanova, G., Smith, C., Araujo, D., and Walter, M.: Trace element composition of silicate inclusions in sub-lithospheric diamonds from the Juina-5 kimberlite: Evidence for diamond growth from slab melts, Lithos, 265, 108–124, https://doi.org/10.1016/j.lithos.2016.08.035, 2016.

Townsend, J. P., Chang, Y.-Y., Lou, X., Merino, M., Kirklin, S. J., Doak, J. W., Issa, A., Wolverton, C., Tkachev, S. N., Dera, P., and Jacobsen, S. D.: Stability and equation of state of post-aragonite BaCO$_3$, Phys. Chem. Miner., 40, 447–453, https://doi.org/10.1007/s00269-013-0582-8, 2013.

Villiers, J. P. R. D.: Crystal structures of aragonite, strontianite and witherite, Am. Mineral., 56, 758–767, 1971.

Wang, M., Liu, Q., Nie, S., Li, B., Wu, Y., Gao, J., Wei, X., and Wu, X.: High-pressure phase transitions and compressibilities of aragonite-structure carbonates: SrCO$_3$ and BaCO$_3$, Phys. Chem. Miner., 42, 517–527, https://doi.org/10.1007/s00269-015-0740-2, 2015.

Wirth, R., Kaminsky, F., Matsyuk, S., and Schreiber, A.: Unusual micro- and nano-inclusions in diamonds from the Juina Area, Brazil, Earth Planet. Sc. Lett., 286, 292–303, https://doi.org/10.1016/j.epsl.2009.06.043, 2009.

Zhang, Y.-F., Liu, J., Qin, Z.-X., Lin, C.-L., Xiong, L., Li, R., and Bai, L.-G.: A high-pressure study of PbCO$_3$ by XRD and Raman spectroscopy, Chinese Physics C, 37, 038001, https://doi.org/10.1088/1674-1137/37/3/038001, 2013.

Zucchini, A., Prencipe, M., Belmonte, D., and Comodi, P.: Ab initio study of the dolomite to dolomite-II high-pressure phase transition, Eur. J. Mineral., 29, 227–238, https://doi.org/10.1127/ejm/2017/0029-2608, 2017.